

JGR Planets

RESEARCH ARTICLE

10.1029/2018JE005805

Key Points:

- Monte Carlo models were performed of the diffusion of H in the Moon's surface and subsequently degassed the H₂ exosphere
- A distribution of activation energies is used to characterize the physical/chemical trapping of H to estimate the OH surface inventory
- The model is consistent with the global OH surface concentration and H₂ exospheric densities observed by M³ and LAMP, respectively

Supporting Information:

- Supporting Information S1
- Data Set S1
- Data Set S2
- Data Set S3
- Data Set S4
- Data Set S5
- Data Set S6
- Data Set S7
- Data Set S8
- Data Set S9

Correspondence to:

O. J. Tucker,
orenthal.j.tucker@nasa.gov

Citation:

Tucker, O. J., Farrell, W. M., Killen, R. M., & Hurley, D. M. (2019). Solar wind implantation into the lunar regolith: Monte Carlo simulations of H retention in a surface with defects and the H₂ exosphere. *Journal of Geophysical Research: Planets*, 124. <https://doi.org/10.1029/2018JE005805>

Received 27 AUG 2018

Accepted 20 DEC 2018





Accepted article online 29 DEC 2018

©2018. The Authors.

This is an open access article under the terms of the Creative Commons Attribution-NonCommercial-NoDerivs License, which permits use and distribution in any medium, provided the original work is properly cited, the use is non-commercial and no modifications or adaptations are made.

This article has been contributed to by US Government employees and their work is in the public domain in the USA.

Solar Wind Implantation Into the Lunar Regolith: Monte Carlo Simulations of H Retention in a Surface With Defects and the H₂ Exosphere

O. J. Tucker¹ , W. M. Farrell¹ , R. M. Killen¹ , and D. M. Hurley² 

¹NASA Goddard Space Flight Center, Greenbelt, MD, USA, ²John Hopkins Applied Physics Laboratory, Laurel, MD, USA

Abstract The solar wind implants protons into the top 20–30 nm of lunar regolith grains, and the implanted hydrogen will diffuse out of the regolith but also interact with oxygen in the regolith oxides. We apply a statistical approach to estimate the diffusion of hydrogen in the regolith hindered by forming temporary bonds with regolith oxygen atoms. A Monte Carlo simulation was used to track the temporal evolution of bound OH surface content and the H₂ exosphere. The model results are consistent with the interpretation of the Chandrayaan-1 M³ observations of infrared absorption spectra by surface hydroxyls as discussed in Li and Milliken (2017, <https://doi.org/10.1126/sciadv.1701471>). The model reproduced the latitudinal concentration of OH by using a Gaussian energy distribution of $f(U_0 = 0.5 \text{ eV}, U_w = 0.078\text{--}0.1 \text{ eV})$ to characterize the activation energy barrier to the diffusion of hydrogen in space weathered regolith. In addition, the model results of the exospheric content of H₂ are consistent with observations by the Lyman Alpha Mapping Project on the Lunar Reconnaissance Orbiter. Therefore, we provide support for hydroxyl formation by chemically trapped solar wind protons.

Plain Language Summary Understanding the water content in the Moon's surface and its thin atmosphere is of interest for space missions. Water products have been detected in various forms (H₂O and OH) on the Moon, which are not distinguishable in the observations. Herein, we examined the contribution of OH content. The solar wind implants protons (positively charged hydrogen atoms) into the top layers of the lunar soil. The implanted H atoms spread out in the grains interacting with other atoms like oxygen. We estimate the mobility of H atoms as they travel to the surface and escape into the Moon's exosphere (very thin atmosphere). The mobility of hydrogen is hindered because they can interact with other atoms or molecules as they travel in the soil. Some hydrogen will interact with oxygen and form OH. We used a Monte Carlo (probability) simulation to track the variation in the surficial amount of OH on the Moon's surface during day and night and hydrogen released in the exosphere (very thin atmosphere). It is found that considering the effect of a variety of trapping sites (interaction sites), hydrogen mobility is needed to reproduce the content of OH in the surface and hydrogen in the exosphere.

1. Introduction

Before the ground-breaking observations of the lunar OH veneer in 2009 (Clark, 2009; Pieters et al., 2009; Sunshine et al., 2009) pioneering theoretical investigations and experiments proposed that the solar wind (SW) is a dynamic source for delivering hydrogen to the surfaces of rocky bodies without atmospheres (Mattern et al., 1976; Starukhina, 2006; Zeller et al., 1966). In this study, we examine the role of the solar wind as a widespread source of hydrogen and hydroxyl to the lunar surface by quantitatively estimating the SW-derived H (i.e., OH) surface content and the H₂ exosphere densities. In our approach we use a Monte Carlo model to calculate the dynamic buildup of OH over time due to populations of molecules with high activation energy diffusional pathways. To this end, we apply a statistical mechanics approach developed in Farrell et al. (2015, 2017) to estimate the diffusional lifetime of H atoms in the silica surface hindered both by physical defects and by forming temporary bonds with oxygen atoms. The statistical distributions are used within a global Monte Carlo simulation to track the temporal OH surface content and the subsequently degassed H₂ exosphere. Li and Milliken (2017) quantified the global distribution of OH surface content using refined observations of infrared absorptions near 2.8 μm in the surface reflectance by the Moon Mineralogy Mapper (M³) instrument on the Chandrayaan-1 mission. The observations indicate that OH content increases with latitude up to 500–750 parts per million (ppm) at high latitudes, and at low latitudes there appears to be a diurnal variation of up to 200 ppm over the lunar day linked to warmer surface

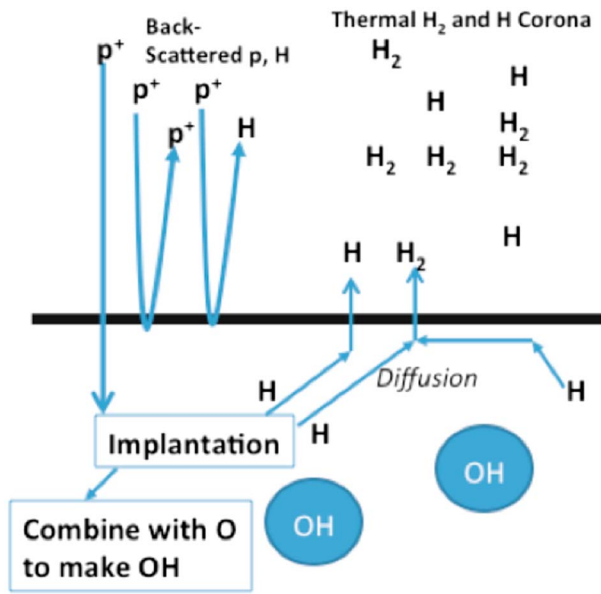


Figure 1. Schematic of proton implantation and the degassed hydrogen corona. Incident SW protons (p^+) implanted in the regolith excite atoms leading to ionization, excited electrons, high-energy neutrals producing various types of physical and chemical defects. The diffusion of H atoms is slowed when they form metastable bonds with oxygen O-H. Direct diffusion of hydrogen and recombinative desorption leading to the formation of H_2 are pathways for hydrogen to degas into the exosphere.

temperatures. The model results are in good agreement both with the global maps of OH surficial content produced from M^3 observations discussed in Li and Milliken (2017) and observations of H_2 in the exosphere by the Lyman Alpha Mapping Project (LAMP) on the Lunar Reconnaissance Orbiter, (Cook et al., 2013; Stern et al., 2013).

1.1. Background

The solar wind is the tenuous plasma emitted from the solar corona. For nominal conditions, the typical flux at Earth is $\approx 2.0 \times 10^8 \text{ cm}^2/\text{s}$, with the composition consisting of primarily protons and electrons, combined with a few percent of He ions and fractional percentages of heavier ions. The protons have energies in the keV range, and the nominal value is typically taken to be 1 keV. Because the Moon does not have a significant global magnetic field, the exposed surface is under constant bombardment by the solar wind particles, except for ~ 5 days when the Moon is in the geomagnetic tail. When the protons penetrate the surface, they are neutralized after undergoing several interatomic collisions while penetrating regolith grains. The penetration or implantation depth depends on the energy of the incident ion, the angle of incidence, and the composition of the target surface and is typically about 20 nm for a 1 keV proton (Farrell et al., 2017). During this process, SW ions energize atoms and molecules via momentum transfer events and excite electrons along its path (Johnson, 1990). On the other hand, the concomitant radiation damage creates physical and chemical trapping sites that also hinder the mobility of hydrogen (Fink et al., 1995; Starukhina, 2006, 2012; Zeller et al., 1966).

Lunar soils are predominantly composed of olivine $(\text{Mg, Fe})_2\text{SiO}_4$, pyroxene $(\text{Ca, Mg, Fe})\text{SiO}_3$ and plagioclase feldspars $(\text{Ca, Na})\text{Al}_2\text{Si}_2\text{O}_8$ (Williams & Jadwick, 1980). Down to 60 cm below the surface the bulk density of the regolith is estimated to be in the range of 1,500–1,800 kg/cm^3 . Oxygen and silicon are the two most abundant elements accounting for an average atomic weight percent of $\sim 60\%$ and $\sim 16\%$, respectively (Turkevich, 1973). Typically, they are in the form of silica (SiO_2) with wt. % ~ 45 (McKay et al., 1991).

Experiments have shown that when silica is irradiated, an infrared absorption feature, near $2.8 \mu\text{m}$, grows as the result of hydroxyl (OH) production (Fink et al., 1995; Griscom, 1984; Zeller et al., 1966). The absorption feature has been attributed to a combination of permanent and metastable hydroxyls present in the silica (Fink et al., 1995; Lee, 1963, 1964). It appears that this process is occurring on the Moon due to solar wind-implanted hydrogen as observed by three independent spacecraft missions (Clark, 2009; Pieters et al., 2009; Sunshine et al., 2009). Within regolith grains implanted hydrogen is present in atomic form and combined with various molecular species. As shown in Figure 1, implanted protons diffuse and can chemically combine with other regolith atoms, like oxygen, or become trapped in physical defects. This process is driven by the energy deposited along the path of penetrating protons that energizes atoms leaving the regolith oxides with dangling bonds (Griscom, 1984; Zeller et al., 1966). Subsequently, the interstitial diffusion of hydrogen is hindered through forming permanent and metastable bonds with regolith oxides. For example, in pristine silica (damage free), hydrogen has a derived diffusion coefficient with a preexponential factor of $D_0 \sim 10^{-9} \text{ m}^2/\text{s}$ (Lee, 1963); however, experiments of diffusion in irradiated silica indicate that the mobility of hydrogen is significantly reduced in damaged SiO_2 , for example, $D_0 \sim 10^{-12} \text{ m}^2/\text{s}$ (in Fink et al., $D(U = 0.52 \text{ eV}, T = 350 \text{ K}) = D_0 \exp(-U/T) \sim 10^{-19} \text{ m}^2/\text{s}$).

One pathway for thermal hydrogen to leave the surface is as molecular hydrogen through recombinative desorption (Starukhina, 2006). In this process, the diffusing H atoms escape the surface binding potential by combining with another H via the sharing of valence electrons. The resultant H_2 molecule has enough kinetic energy to escape the 1–2-eV surface binding energy (Starukhina, 2006). Observations of the H_2 lunar exosphere obtained with LAMP are consistent with this hypothesis (Hurley et al., 2016; Stern et al., 2013). Additional observations of energetic neutral H (Wieser et al., 2009) and methane (Hodges, 2016) suggest

that H atoms can find a variety of pathways to escape the surface potential, but molecular hydrogen appears to be the dominant pathway.

1.2. Lunar Observations of Surface Hydrogen and the H₂ Exosphere

Hydroxyl groups have been identified on the Moon by observation of infrared absorption features in the wavelength range of near $\sim 2.8 \mu\text{m}$ (Clark, 2009; Pieters et al., 2009; Sunshine et al., 2009). Sunshine et al. (2009) reported on observations by the Deep Impact (DI) High-Resolution Instrument-infrared spectrometer of absorption features at low latitudes $20\text{--}60^\circ\text{N}$ that indicated a diurnal dependence of water content with the strongest absorptions occurring near the terminators. From morning to noon, the band depth decreased by $\sim 70\%$. At high latitudes $>70^\circ\text{N}$ the strongest absorption features were observed but with less diurnal variation. Li and Milliken (2017) constructed the first quantitative global maps of OH content from M³ observations that were consistent with the DI findings. They found that the water content varied by 200 ppm over the lunar day at latitudes between $\sim 30^\circ$ and 70° . However, at latitudes above 70° and below 30° a diurnal variation was not identifiable. The maximum content of $\sim 500\text{--}750$ ppm was observed in the Northern Hemisphere at latitudes above 70° with values consistently larger than that in the Southern Hemisphere, whereas below 30° the surficial OH content was constrained to values $< \sim 100$ ppm (Li & Milliken, 2017).

In warmer regions the loosely bound surficial hydrogen attached to a metastable OH (Fink et al., 1995) is possibly outgassed as H₂ (Starukhina, 2006). Stern et al. (2013) reported on a substantial H₂ exosphere with densities between $1,200$ and $9,000 \text{ cm}^{-3}$. Both LAMP and the Apollo 17 orbiter both performed UV observations of the exosphere constraining the near-surface atmospheric density to $< 9,000 \text{ cm}^{-3}$ (Feldman & Morrison, 1991). Cook et al. (2013) analyzing LAMP spectra noted a dusk to dawn asymmetry of $1,700 \pm 400$ and $2,100 \pm 300 \text{ cm}^{-3}$, respectively. Partial pressures measured by the Chandrayaan-I Chandra's Altitudinal Composition Explorer (CHACE) mass analyzer were used to infer near-surface densities of $500\text{--}800 \text{ cm}^{-3}$ (Thampi et al., 2015). In that study, the estimate of the neutral densities depended on the assumption of the surface temperature. Indirectly, the Neutral Mass Spectrometer (NMS) on the Lunar Atmosphere and Dust Environment Explorer inferred consistent neutral densities by detecting H₂ ions produced by photoionization (Halekas et al., 2015).

1.3. Experimental and Theoretical Studies

Starukhina (2006) predicted that solar wind elements are favorably retained at high latitudes by investigating the diffusional timescales of implanted hydrogen. The steady state concentration of atoms was balanced by incident solar wind flux using Fick's first law $j = -D(dn/dz)$, where j is the diffusive flux, $D = D_0 \exp(-U/T)$ is the diffusion coefficient (m^2/s), D_0 is a preexponential factor, U is the activation energy, T is temperature in eV, and dn/dz is the concentration gradient. From Fick's first law the diffusive flux in terms of the total density, n , within the implantation layer of depth, h , is approximated by equation (1).

$$j \approx D(U, T)nh^{-1} \quad (1)$$

From equation (1) an approximate timescale for diffusive loss can be defined as $\tau_1 = h^2/D(U, T)$; e.g., Starukhina, 2006). As described in Starukhina (2006), the degassing rate decreases significantly in cooler regions due to the exponential dependence on temperature. Therefore, at high latitudes where the surface has a high U/T ratio more hydrogen is accumulated even though the solar wind flux is lower. In contrast, at low latitudes hydrogen is more easily degassed even though the solar wind flux is higher because the U/T ratio is lower and $D_0 \exp(-U/T)$ is larger. Starukhina (2006) emphasized that the lunar surface would have a broad range of activation energies characteristic of trapping by a variety of physical and chemical defect sites. Estimates of the diffusional lifetime for atoms trapped physically and chemically are given in Table 1. The lifetimes were evaluated using the τ_1 with $D_0 = 10^{-6} \text{ m}^2/\text{sand}$ $h = 100 \text{ nm}$ from Farrell et al. (2015). Within crystalline SiO₂, the energy barrier to vacancy diffusion and H bound in OH groups is $\sim 1\text{--}3$ eV. This barrier to diffusion of H bound in OH groups is high compared to the thermal energy of surface bound atoms ~ 0.03 eV, (Starukhina, 2006). However, diffusion via interstitial hopping and along grain boundaries is more favorable (energy barrier $\lesssim 0.1$ eV) due to increased interatomic spacing and lower atomic binding energies. Starukhina (2006) estimated that activation energies of $U \gtrsim 1.3$ eV and $U \gtrsim 0.8$ eV for the lunar surface at low and high latitudes, respectively, are required to trap hydrogen concentrations

Table 1
Residence Time Associated With Various Defects

T(K)	* $U_{V\&CB} = 1.0$ eV	⁺ $U_{Int\&GB} = 0.5$ eV
180	>> Gyrs	12 days
280	31 decades	10 s

*Vacancies and chemical bonds. ⁺Interstitial sites and grain boundaries.

on the order of $\lesssim 160$ ppm. Therefore, it was suggested that vacancy and chemical trapping would be required to build up the H concentration at low latitudes, whereas even physical trapping could be important at high latitudes.

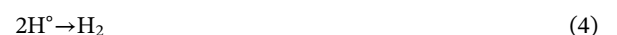
It is well known in the silicon microelectronics industry that material defects significantly alter the diffusive properties of silica. Impurities in natural silica alter the spacing between oxygen atoms, which in turn affect the local electron cloud, and the covalent bonds within OH groups. This

population of hydroxyls is commonly referred to as *metastable* (Fink et al., 1995; Lee, 1964). The existence of metastable OH has been inferred from experiments of loading H₂ gas to silica samples and subsequent annealing (Devine, 1985; Lee, 1963, 1964; Shelby & Keeton, 1974). Lee (1963) found the IR absorption feature about 2.75 μm became deeper and more broadened during experiments that loaded H₂ gas to silica laden with impurities at temperatures of 900 K–1,100 K. Upon degassing in vacuum at $T \sim 1,073$ K, it was found that the IR absorption feature was removed. However, when the same treatment was applied to highly pure samples, it did not produce any significant change in their respective OH feature. Later, Lee (1964) using experimental data from IR (absorption feature) and mass (H₂ degassing rates) spectrometers showed that the amount of metastable OH could significantly outnumber the amount of permanent OH in samples. For example, they reported a metastable OH content of ~ 100 ppm compared to < 5 ppm of permanent OH in an experiment annealed at 1,100 K. It was concluded that samples with impurities possessed populations of both free hydroxyl characteristic of strong O-H bonds with a well-defined potential minimum and metastable O-H bonds characterized by potential wells of varying depth.

Experiments performed under conditions more applicable for the lunar environment have shown that metastable O-H is also produced during irradiation of silica at low temperatures (Griscom, 1984; Fink et al., 1995; Zeller et al., 1966). Zeller et al. (1966) irradiated silica glass with protons and found strong evidence for the enhancement of the OH absorption feature as seen by a monotonic increase of the optical density of the feature with increasing flux. Furthermore, it was observed that with increasing dosage, the optical density approached a constant, thus, indicating that irradiation was both producing and destroying OH. Zeller et al. found that up to 100% of the implanted H could be converted into OH at the onset of bombardment. When a similar experiment was performed with helium and hydrogen-2 ions, no significant increase in optical density was observed.

Fink et al. (1995) performed experiments of hydrogen implantation and diffusion in silica annealed in the temperature range of 320 K–550 K. Permanent OH is not removable by degassing at these temperatures (Lee, 1964). However, the Fink et al. experiments demonstrated that ion irradiation also enhances diffusion. That is, irradiation at low temperature leads to a dynamic equilibrium between the formation of dangling bonds (immobile atoms with an unsatisfied valence) and diffusing hydrogen (H, H₂; Fink et al. 1995; Griscom, 1984). The dangling bonds become trapping sites for interstitially diffusing hydrogen.

Similar results have been obtained during experiments of X-ray irradiation of silica at temperatures of $100 \text{ K} < T < 300 \text{ K}$ (Griscom, 1984; Revesz, 1979, and references therein). Griscom (1984) reviewed electron spin resonance experiments of silica samples with 1,200 ppm of hydroxyl irradiated by hard X-rays and subsequently annealed at 77 K and 100 K. These works inferred that the production/destruction of metastable hydroxyl occurred via the following reactions (Griscom, 1984):



where (.) and (o) represent a valence electron and electron hole, respectively. The reaction in equation (2) proceeds to the right under irradiation and to the left during annealing. Griscom (1984) showed for such samples that the reaction in equation (3) is limited by diffusion, as the reaction rate occurs more than 4 orders of magnitude faster than the diffusion rate. Various studies examining the mobility of hydrogen in silica have shown that diffusion was best characterized by using a distribution of activation energies to represent the random sizes and of interstitial and trapping sites in irradiated silica (Devine, 1985; Griscom, 1984;

Shelby & Keeton, 1974). The mean activation energies derived from (H, H₂) diffusion in various pristine and amorphous silica samples ranges from 0.18 to 0.73 eV (Fink et al., 1995, their Figure 6).

2. Methods

Here we model the experimental and theoretical approaches of hydrogen diffusion discussed in Fink et al. (1995) and Starukhina (2006). That is, the implanted hydrogen diffuses by hopping from O to O in the bound SiO₂-rich regolith. The O then *hinders* the H diffusion (Fink et al., 1995), to form metastable OH. Once on the surface, the mobile H atoms find each other and leave the surface via recombinative desorption H + H = H₂. Therefore, a dynamic equilibrium exists between the diffusion of atoms and molecules slowed by trapping in defects and the subsequently degassed molecular hydrogen to the exosphere.

Farrell et al. (2015) showed that using a distribution of activation energies to characterize hydrogen retention in the regolith could simulate the observed diurnal variation of the IR absorption feature. As discussed therein, it is expected that implanted H atoms would have a range of activation energies in space-weathered grains due to variable interatomic spacing. Each atom can be considered to have activation energy dependent on its individual diffusion path but characteristic of a mean value. Without knowledge of this distribution a priori, a Gaussian distribution of energies was used to characterize both populations of atoms that are easily outgassed and those that are trapped for long time periods.

The Gaussian distribution has the form of

$$F(U) = \frac{n}{U_w \sqrt{\pi}} \exp \left[\frac{-(U-U_0)^2}{U_w^2} \right] \quad (5)$$

where U_0 is the energy of the peak of the distribution and U_w is the width about the peak. Over timescales much less than the diffusive timescale, a quasi-steady state density of implanted H atoms can be obtained using the continuity equation:

$$\frac{dn}{dt} = \frac{\langle D(U, T)n \rangle}{h^2} - \frac{n_{sw} v_{sw} \cos(Z)}{h} \sim 0 \quad (6)$$

where n_{sw} and v_{sw} are the solar wind density and velocity respectively and Z is the solar zenith angle (Farrell et al., 2017). In equation (6) the diffusive flux is defined in terms of a mean value because of the use of the Gaussian distribution $\langle j \rangle = \langle \frac{Dn}{h} \rangle = D_0 h^{-1} \int \exp(-U/T) F(U) dU$. Upon integration over all energies, an effective diffusion coefficient is obtained $D_{eff} = D_0 \exp(-U_0/T) \exp(U_w^2/4T^2)$. Similar approaches have been used in the studies of hydrogen diffusion in silica glass (Devine, 1985; Shelby & Keeton, 1974). Using equation (6), Farrell et al. (2017) define an analytical expression of the implanted density as a function of solar zenith angle assuming dynamic equilibrium on timescales much less than a lunation:

$$nv \sim n_{sw} v_{sw} \cos(Z) \quad (7)$$

where $v = D_0 h^{-1} \exp(U_0/T) \exp(-(U_w^2)/4T^2)$ is defined as the diffusive velocity, or in terms of a diffusive lifetime $\tau_2 = h/v = D^{-1} h^2 \exp(U_0/T) \exp(-(U_w^2)/4T^2)$. A comparison of expressions of τ_2 and τ_1 or D_{eff} and D shows that the diffusion rate is decreased by the factor of $\exp(-(U_w^2)/4T^2)$ when considering a distribution of activation energies. This is due to the fraction of the distribution that possesses activation energies less than the mean value of $U < U_0$, which is characterized by the width of the distribution, U_w , as shown in Figures 2a and 2b. On the other hand, 50% of the distribution also has $U > U_0$, and therefore, over long time periods the net result is an increase in the surface concentration compared to the monoenergetic case, as shown in Figure 2c. That is, over time atoms and molecules with high activation energies will dominate the surface concentration.

We used the Monte Carlo approach to track the diffusion lifetimes of hydrogen atoms in the surface. In Figure 2a, we show a contour map of the surface concentration calculated with equation (7) using the parameters $U_0 = 0.5$ eV and $U_w = 0.1$ eV. As discussed, the concentration is largest in cooler regions along the terminator. The analytical solution assumes dynamic equilibrium. At solar zenith angle of 0° and 89° the volumetric surface concentration is 6×10^{21} and 2×10^{23} H/m³, respectively, where the subsolar point is

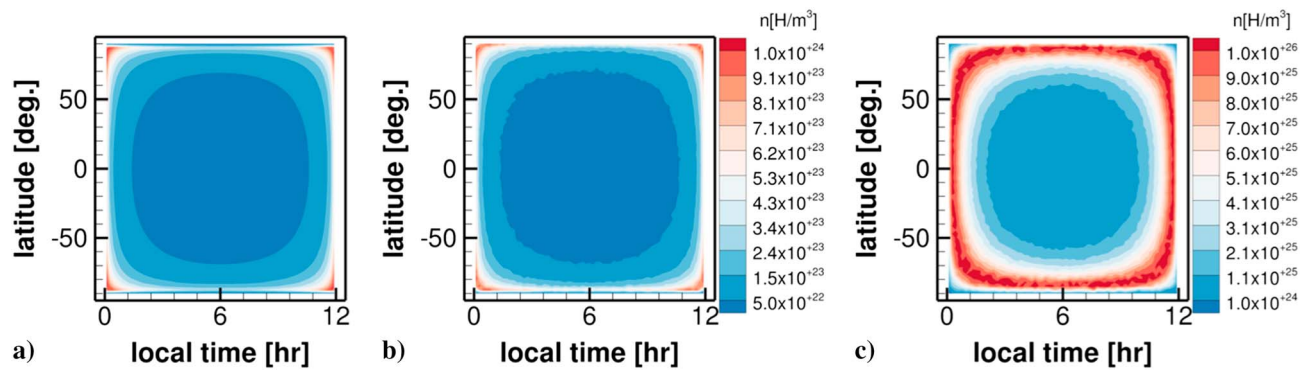


Figure 2. (a) Contour of analytical solution from equation (7) of steady state hydrogen surface concentration assuming dynamic equilibrium. (b) Monte Carlo simulation comparison for same time constraint. (c) Monte Carlo result after accumulation over several lunations.

defined at 0° latitude and local time 6 hr. As discussed below in section 2.1, each implanted atom was assigned a random implantation depth and activation energy. These values are then used to calculate the diffusion lifetime on an implantation-by-implantation basis. This lifetime is used to make a Monte Carlo choice to determine if an H_2 molecule escapes the surface. In Figure 2b we plot the bulk average H concentration using an energy-averaged diffusion time based on the Monte Carlo implantations in a given region. The activation energy-averaged numerical Monte Carlo model and the activation energy-integrated analytical result are shown to be consistent for timescales much shorter than a lunation, providing a check that the model was performing as expected.

Subsequent modeling of timescales longer than a lunation resulted in a buildup of surface concentration because not all of the implantations contribute to an immediate dynamic equilibrium over the lunar day. Given the distribution of activation energy with $U_0 = 0.5$ eV and $U_w = 0.1$ eV, those few atoms with energies at the high-energy tail of the distribution can remain trapped over periods longer than a lunation. These populations of trapped H atoms accumulate with time, and the accumulated effect of this small but ever-growing population is shown in Figure 2c. Hence, while a dynamic equilibrium condition applies in warm regions to most of the H atoms undergoing diffusion, in cooler regions there is a population of high U valued implantations that accumulate and dynamic equilibrium does not apply.

After diffusing to the surface, many hydrogen atoms leave in a molecular form to escape the surface potential (Starukhina, 2006). This is supported by Apollo era measurements that place an upper limit of ~ 10 cm $^{-3}$ of thermal atomic hydrogen in the exosphere. Ground-based and remote observations indicate that the dominant pathway of hydrogen loss from the surface is in the form of molecular hydrogen (Cook et al., 2013; Hodges, 1973; Stern et al., 2013). Helium measurements, which have been well characterized, strongly suggest that nonthermal sources produced by micrometeoroid impacts and sputtering are not significant (Hodges, 1973). Therefore, the source hydrogen to the exosphere depends on the diffusion of hydrogen and its conversion into H_2 within the surface. To this end, we have examined diffusion-limited degassing as the limiting factor to the exosphere. The advantage to this Monte Carlo approach is that both the population of hindered H atoms can be tracked and those that are lost in the H diffusion and H_2 escape process (H- H_2 pathway).

2.1. Model Description

We have adapted the Monte Carlo model applied in Tucker et al. (2015) to the Moon in order to track the surface inventory of atomic hydrogen and subsequently degassed molecular hydrogen to the exosphere. The computational domain is centered on the Moon and discretized in spherical coordinates in the azimuth and zenith angles using 8,000–20,000 surface elements. The corresponding surface areas ranged from 45 to 6,600 km 2 from the poles to the equator. In the radial direction we used a nonlinear grid composed of spherical cells. The exosphere grid was discretized into 60,000 cells with volumes of 40,000– 3×10^6 km 3 with the lower volumes corresponding to cells near the surface and the larger for cells near outer boundary of $\sim 6,000$ km. Each cell was given a radial width chosen to be a fraction of the scale height corresponding to

the lowest surface temperature of 100 K. We used an inertial frame of reference centered on the Moon, and the surface temperature was calculated using $T(Z) = 280 \text{ K} \cdot \cos^{1/4}(Z) + 100 \text{ K}$ (Butler, 1997; Crider & Vondrak, 2000). At temperatures of 100 K–380 K the mean thermal speed of H_2 ranges from ~1,000–2,000 m/s. Based on the ratio of the lowest radial cell width divided by the thermal speed, we obtained a time step on the order of tens of seconds. The integration period for averaging macroscopic properties during the simulation was limited to time intervals <10 min, so that molecules traveled distances less than a scale height per integration period. More detailed models could include the effect of the lunar rotation in the Earth-Sun system. For simplicity, we have used an inertial frame of reference and considered only the near-surface exosphere. The Moon's rotation in a three-body system results in 1–2° variation of subsolar point (e.g. Tenishev et al., 2013). However, including such effects would not alter the conclusions of this study.

For the solar wind we applied typical conditions of density $n_{\text{sw}} = 5 \times 10^6 \text{ H/m}^3$ and speed $v_{\text{sw}} = 400 \text{ km/s}$. The local flux incident to each surface element is estimated using its zenith angle with $n_{\text{sw}} v_{\text{sw}} \cos(Z)$ assuming that the Sun is in the z -plane. The implanted atoms and exospheric molecules are represented statistically by using a particle weight. The particle weight was derived from the SW flux so that each computational particle represented 10^{24} implanted hydrogen atoms. Leveraging the studies of Farrell et al. (2015, 2017) each implanted particle was given an activation energy, U , selected from a Gaussian energy distribution (equation (5)) using a Monte Carlo choice. Likewise, each atom was also prescribed a random depth, h , chosen from a Gaussian distribution based on TRIM profile. Then at each integration step, the diffusion lifetime was determined using $\tau_{\text{num}} = D_0^{-1} h^2 \exp(U/T)$ by evaluating the probability for an implanted particle to degas as $r > \exp(-dt/\tau_{\text{num}})$, where r is a uniformly distributed random number ranging from 0 to 1. We considered that all surface loitering hydrogen bond (permanently or metastable) with oxygen in order to obtain an upper limit estimate of the hydroxyl surface concentration. We did not directly consider the effect of the reaction rate of H in regolith oxides, which is another limiting factor to the production of OH. However, based on the hydroxyl observations of 10–1,000 ppm a lower bound estimate of the reaction times is on the order of $> \sim 50 \text{ s}$ and $> \sim 1 \text{ day}$ for the subsolar point and terminator regions, respectively (Farrell et al., 2015).

Guided by previous experimental work as discussed in section 1.3, our approach examined the effect of diffusion on the exospheric hydrogen budget. Therefore, to estimate an upper limit of the molecular hydrogen density, we assumed that all particles escaped as H_2 by reducing the degassed particle weight by half. This is equivalent to removing two hydrogen atoms from the surface inventory. The degassed molecules were assigned a random velocity determined from the local surface temperature. Therefore, we emitted molecules into the exosphere using a thermal speed randomly selected from the Maxwell-Boltzmann flux-speed distribution (Brinkmann, 1970), and the velocity vector was directed with a cosine distribution about the surface normal. The upper radial bound of the grid was specified to be 5–10 scale heights above the surface. If a molecule traversed the upper boundary with a speed larger than the escape speed, it was removed from the simulation. Otherwise, the molecule was tracked until it returned ballistically back into the averaging domain. We also tracked the shadow of the Moon projected onto the exosphere to consider photo-induced losses. The lifetime of H_2 against photodestruction is taken to be $\tau_{\text{photo}} \sim 6.8 \times 10^6 \text{ s}$ (2.5 months) from Huebner and Mukherjee (2015). Even though there was a probability for molecules to be lost from photochemical processes, $r > \exp(-dt/\tau_{\text{photo,ADS}})$, the primary loss mechanism was thermal escape. We did not consider the lifetime for H_2 adsorbed on the surface because above ~15 K its sticking probability approaches 0 (Acharyya, 2014; Penteadó et al., 2017).

3. Results

3.1. Surface Concentration

Three case studies were simulated using a Gaussian activation energy distribution each defined with a different mean energy of $U_0 = 0.3, 0.7, \text{ and } 0.5 \text{ eV}$, respectively, for comparison to Farrell et al. (2015, 2017). In the Farrell et al. studies a range of mean activation energies was considered to characterize surfaces defined with $U_0 < 0.3 \text{ eV}$ as emissive, $U_0 > 0.9 \text{ eV}$ as retentive, and $0.3 \text{ eV} < U_0 < 0.9 \text{ eV}$ as diurnal varying. Emissive surfaces degassed their hydrogen content in less than a lunation, whereas retentive surfaces possessed more high activation energy trapping sites retaining atoms longer than a lunation period. For the

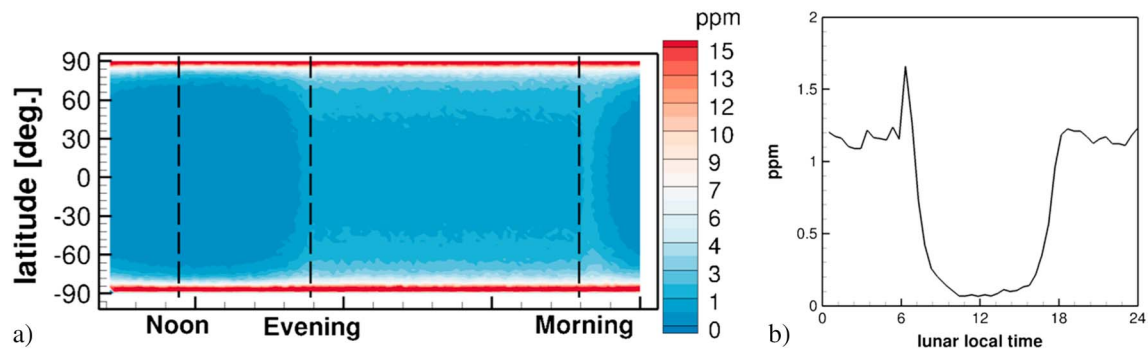


Figure 3. (a) $f(U_0 = 0.3 \text{ eV}, U_W = 0.1 \text{ eV})$ snapshot contour of dynamic surface concentration over the lunar surface as a function of lunar local time. The dashed lines identify the location of the morning and evening terminators and local noon. (b) Diurnal surface concentration extracted from (a) along 0° latitude.

intermediate energy range Farrell et al. (2015) found that the surface concentration could vary diurnally. However, these previous studies considered the dynamic buildup of the hydrogen surface concentration on timescales much smaller than a lunation. Here we simulate the dynamic buildup of hydrogen over several lunations. The adjustable parameters are D_0 , U_0 , and U_W for the activation energy distribution and h_0 and h_W for the implantation depth. To this end, we used parameters derived/inferred from experiments and theoretical studies: $U_W = 0.1 \text{ eV}$, $D_0 = 10^{-12} \text{ m}^2/\text{s}$, $h_0 = 20 \text{ nm}$, and width in the implantation distribution of $h_W = 13 \text{ nm}$ (Farrell et al., 2017; Fink et al., 1995; Griscom, 1984; Shelby & Keeton, 1974; Starukhina, 2006; Zeller et al., 1966). The simulations were started without any implanted H atoms, and we simulated the progression to a quasi-steady state. In order to obtain an upper limit estimate of the hydroxyl content, it was assumed that all implanted hydrogen paired with oxygen to form a metastable O-H pair like that defined in Fink et al. (1995). We calculated distributions of the surface content as a function of latitude and local lunar time. The results of the three simulation cases are presented below in parts per million (ppm) calculated using a regolith density of $1,700 \text{ kg/m}^3$.

Case Study 1, $f(U_0 = 0.3 \text{ eV}, U_W = 0.1 \text{ eV})$: Result for the activation energy distribution centered at 0.3 eV with width 0.1 eV is shown Figure 3. For this distribution Farrell et al. (2015) obtained a result for which no atoms were retained during 8:00 am to 12:00 pm (lunar local time) at the equator, and at 80° latitude only 0.2% of atoms were retained. We note that Farrell et al. (2015) used a much larger $D_0 = 10^{-6} \text{ m}^2/\text{s}$ derived from diffusion experiments with pristine silica. For comparison we show our result obtained with the same energy distribution in Figure 3a but using the smaller preexponential factor of the diffusion coefficient derived from the Fink et al. (1995) experiments of diffusion in irradiated silica glass. We obtained a quasi-steady state concentration balanced by the SW flux after two lunations. At latitudes below $\sim 85^\circ$, the surface concentration was balanced by the degassing of H_2 molecules and implanted solar protons during the lunar day. On the illuminated surface the concentrations below this latitude were nearly uniform with values $< \sim 1 \text{ ppm}$. Above this latitude, independent of the local lunar time, there was a net accumulation on the order of $\sim 19 \text{ ppm}$ (OH) after 18 lunations, Figure 3a. However, it is expected that eventually, the surface concentration at high latitudes will reach dynamic equilibrium as well (discussed below in section 3.3). Figure 3a shows a diurnal variation that is largest near midlatitudes $\sim 45^\circ$. While a time of day dependence is also obtained at low latitudes, the variation is not very significant, Figure 3b. The surface concentration was largest at the morning terminator because of the addition of freshly implanted atoms added to the concentration of atoms retained over the lunar night. Because most atoms degassed during the day (14 Earth days), the concentrations were lower at the evening terminator compared to morning. The day/night asymmetry obtained in our study was solely due to implantation and not the migration of hydrogen above the surface.

Case Study 2, $f(U_0 = 0.7 \text{ eV}, U_W = 0.1 \text{ eV})$: Result for the activation energy distribution centered at 0.7 eV with width 0.1 eV is shown in Figure 4. This distribution results in retention times that exceed several lunations for a significant fraction of the implanted atoms. Therefore, the very large surface concentration (much larger than reported in Li & Milliken, 2017) is mostly reflective of the solar wind source. As shown in Figure 3a, the concentration increases from the poles with decreasing latitude to $\sim 40^\circ$. However, at lower latitudes the accumulation is partially slowed due to the increased degassing occurring from the warmer surface regions. Although the residence time at local noon is less than a lunation for implanted atoms with

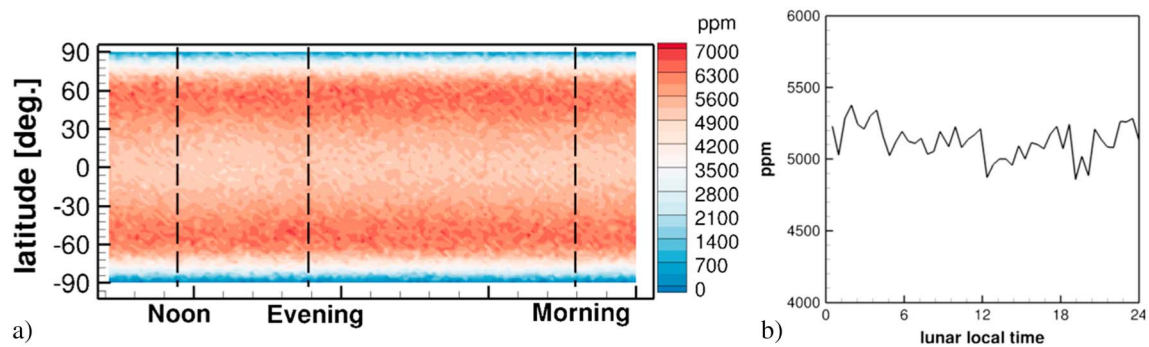


Figure 4. (a) $f(U_0 = 0.7 \text{ eV}, U_W = 0.1 \text{ eV})$ snapshot contour of dynamic surface concentration over the lunar surface as a function of lunar local time. The dashed lines identify the location of the morning and evening terminators and local noon. (b) Diurnal surface concentration extracted from (a) along 0° latitude.

$U = 0.7 \text{ eV}$, atoms with higher activation energies stick around longer and the cumulative effect over several lunations masks any diurnal variations, for example, Figure 4b.

Case Study 3, $f(U_0 = 0.5 \text{ eV}, U_W = 0.1 \text{ eV})$: Result for the energy distribution centered at 0.5 eV with width 0.1 eV is shown in Figure 5. The snapshot of the OH concentration after 18 lunations shown in Figure 5a is consistent with the Li and Milliken (2017) globally averaged map constructed from the M^3 observations, for example, their Figure 1a. Farrell et al. (2017) used this same distribution and the preexponential factor to the diffusion coefficient of $D_0 = 10^{-12} \text{ m}^2/\text{s}$ with equation (7) but estimated a dynamic mass fraction that was less than 0.3 ppm at latitudes above 85° for timescales much less than a lunation. Therefore, Farrell et al. showed that if 90% of the diffusing H atoms had an activation energy of 0.5 eV and 10% had an activation energy of 0.7 eV, the amount retained would be $>30 \text{ ppm}$. In contrast, using the Monte Carlo approach with a single activation energy distribution ($U_0 = 0.5 \text{ eV}$), we obtained a much larger OH mass fraction of $\sim 700 \text{ ppm}$ at high latitudes and $\sim 45 \text{ ppm}$ near the subsolar point after 18 lunations. The difference is due to the accumulation of those very slowly diffusing H atoms with higher activation energy that are not in strict dynamic equilibrium during a lunation period. Consistent with Li and Milliken (2017), we obtained concentrations $< \sim 100 \text{ ppm}$ at latitudes up to 30° , and above latitudes of $\sim 70^\circ$ the concentrations were constant with values of $\sim 750 \text{ ppm}$. However, we obtained a diurnal effect even along the subsolar longitude. Li and Milliken noted in their analyses that a clear enhancement between dawn and dusk was not identifiable because the observations of local evening occurred closer to noon than the morning observations. In our study, we obtained a relative enhancement in concentration at dawn compared to dusk due to the summation of atoms retained throughout the night and newly implanted atoms added in the early morning hours. This population represents a fraction of newly implanted atoms with low barriers to diffusion characteristic of physical trapping sites such that they degas during the lunar day. For a surficial point rotating near the equator its concentration increases by $\sim 15 \text{ ppm}$ from 6 to 7 am, followed by a decrease of 65 ppm as it rotates to noon, and finally, there is another increase by 40 ppm as the point rotates to the night. On the cold night side with the source turned off the surface maintains a constant concentration of $\sim 95 \text{ ppm}$. We did not obtain

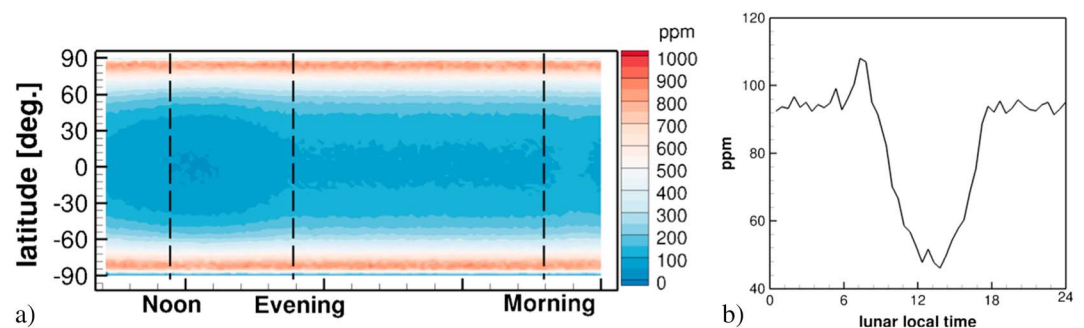


Figure 5. (a) $f(U_0 = 0.5 \text{ eV}, U_W = 0.1 \text{ eV})$ snapshot contour of dynamic surface concentration over the lunar surface as a function of lunar local time. The dashed lines identify the location of the morning and evening terminators and local noon. (b) Diurnal surface concentration extracted from (a) along 0° latitude.

a variation in surface concentration of ~200 ppm at midlatitudes as shown for two spectra in Li and Milliken (2017), their Figures 6c and 6d. Nevertheless, our reported variation is within the range of the standard deviation of the observation.

From the three case studies, we find that the H concentrations match the IR observations for $D_0 = 10^{-12} \text{ m}^2/\text{s}$, $U_0 \sim 0.5 \text{ eV}$, and $U_w \sim 0.1 \text{ eV}$. Activation energies below $U_0 \sim 0.5 \text{ eV}$ tended to release the hydrogen too fast, resulting in low surface concentrations. Values far above 0.5 eV tended to retain the hydrogen, resulting in high surface concentrations and a loss of the latitude and diurnal variations.

3.2. Results: Exosphere Densities

Previous models of the Moon's H_2 exosphere have been presented by Hodges (1973), Hartle and Thomas (1974), Crider and Vondrak (2002), Hurley et al. (2016), and references therein. Hartle and Thomas (1974) used a Monte Carlo model to predict upper limits of H_2 densities to account for degassed hydrogen from solar wind implantation. The model of Hurley et al. (2016) examined solar wind and micrometeoroid sources to demonstrate that chemical sputtering is the most likely source mechanism supplying H_2 in the exosphere. Chemical sputtering refers to solar wind irradiation of the surface that leads to the formation of H_2 , which then degases at the local surface temperature. The release of atoms via chemical sputtering has a lower energy threshold than physical sputtering, being a thermal release. Hurley et al. (2016) reported that source rates in the range of 2.2–17.7 g/s were required to produce near-surface exospheric densities in the range of 1,200–9,000 cm^{-3} .

A key difference of our approach is inclusion of the implantation model. That is, the previous studies derived exospheric source rates of H_2 by constraining models using observations of the exosphere. Here we follow the H to H_2 pathway from solar wind implantation, surface accumulation, and exospheric emission. Following the suggestion of Hurley et al. (2016), we have examined the effect of varying diffusion on exospheric content as a function of temperature. As expected for an exosphere in equilibrium with the surface temperature, the H_2 densities are more extended on the dayside, and largest densities occur near the surface on the nightside (Hodges & Johnson, 1968). On the dayside the exospheric densities peak near the subsolar point where degassing occurs most efficiently. On the nightside the densities peak after local midnight. This is due to the hopping distance of H_2 as molecules near the dawn terminator hop back to the nightside once the surface temperature warms. We obtained similar exospheric densities as described by Hodges and Johnson for the activation energy distributions centered at $U_0 = 0.3 \text{ eV}$ and 0.5 eV because in both cases a significant amount of hydrogen is degassed. However, the density distribution was significantly reduced in the Case Study 2 using the activation energy distribution centered at $U_0 = 0.7 \text{ eV}$. Figure 6 shows the change in exospheric H_2 content in the case of slow diffusion in a highly reactive regolith. The exosphere is in balance between its surface source and escape. The density of the H_2 exosphere is primarily limited by thermal escape, for which H_2 has a lifetime of 4,200 and 9,600 s at the subsolar point and at the terminators ($Z = 89^\circ$), respectively (Johnson, 1971). The diffusion lifetimes range from 4,200 s to 4 days for $U = 0.5 \text{ eV}$. However, for $U = 0.7 \text{ eV}$ the diffusion lifetime can be much larger than thermal escape, for example, 1 day to thousands of years.

We can estimate the activation energy above which the exosphere is increasingly limited by diffusion by equating the thermal escape and diffusion lifetimes. For thermal escape $\tau_{\text{esc}} = \frac{v_m}{g} \frac{\exp(\lambda)}{(1+\lambda)}$, equating $\tau_{\text{esc}} = \tau_1$, we obtain $U_{dl} = T(\text{eV}) \ln \left(\tau_{\text{esc}} \frac{D_0}{h^2} \right) = 0.52 \text{ eV}$, where $v_m = (2\pi kT/m)^{1/2}$, $g = 1.9 \text{ m/s}^2$ is the lunar surface gravity, and $\lambda = \frac{GMm}{rkT}$ is the Jeans escape parameter (Johnson, 1971). For activation energy distributions with mean energies above 0.52 eV the abundance of the exosphere would be limited by diffusion out of the surface. For example, we obtain steady state source rates from the surface to the exosphere of 27 and 13 g/s for the activation energy distribution centered at $U_0 = 0.5 \text{ eV}$ and 0.7 eV , respectively. These loss rates correspond to thermal escape rates of $\sim 8\text{--}9 \times 10^{24} \text{ H}_2/\text{s}$ and $\sim 3\text{--}4 \times 10^{24} \text{ H}_2/\text{s}$, respectively.

3.3. Discussion

Our results are consistent with both the quantity and the trend in diurnal and latitudinal variability of the global distribution of surface concentration as observed by M^3 , Figures 7a and 7b. The observational data were to be adequately reproduced with an activation energy distribution of $f(U_0 = 0.5 \text{ eV}$,

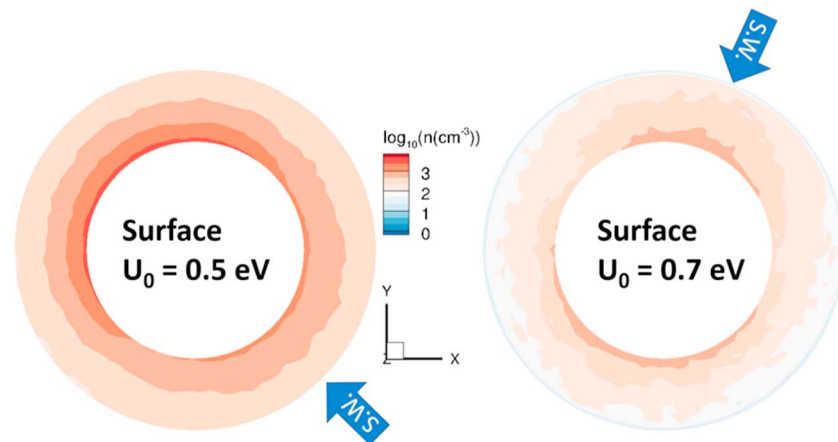


Figure 6. Equatorial slice of exospheric density distribution after 18 lunations from simulation with (left) $U_0 = 0.5$ eV and (right) $U_0 = 0.7$ eV, respectively. The blue arrows indicate the direction of the solar wind.

$U_W = 0.078\text{--}0.1$ eV). This distribution is mitigated both by the change in U/T with latitude and throughout the lunar day (e.g., Farrell et al., 2017) and the magnitude of the SW flux. The diurnal change in surface temperature is an important driver at low latitudes, and the effective activation energy and SW flux are important at high latitudes. We have shown this diurnal variation results from atoms with diffusive lifetimes longer than the lunar night being retained and then degassing throughout the lunar day as the surface temperature increases. In general, we obtain a maximum in surface concentration near $\sim 80^\circ$; above this latitude the concentrations decrease due to the lower SW flux. A similar trend is seen in Li and Milliken (2017), for example, their Figure 1(c); however, the observations were specified as having a low signal-to-noise ratio.

A question is whether the longer-lived metastable O-H pairs have potential structures to accommodate the vibrational modes. Lee (1963) found that diffusion, hindered hydrogen through quartz could create these metastable O-H pairs that had potentials deep enough to accommodate the vibration mode—with an $\sim 3\text{-}\mu\text{m}$ IR detection from the material. By analogy, we would expect the diffusing H atoms, jumping from O to O in the material (Starukhina, 2006) to also create the $3\text{-}\mu\text{m}$ IR band depth feature.

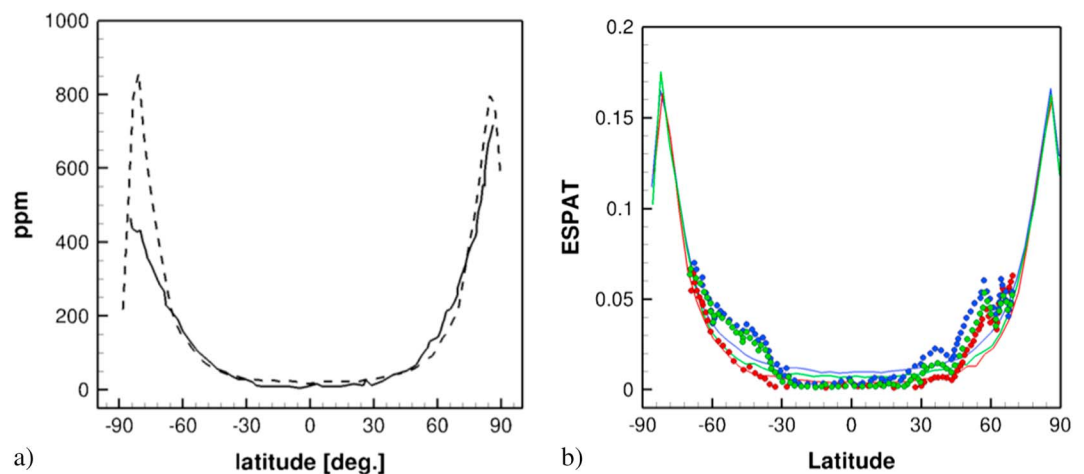


Figure 7. (a) M^3 mean surface concentration plotted as a function of latitude (black curve) compared to the Monte Carlo results at noon (dashed curve) using activation energy distribution of $f(U_0 = 0.5$ eV, $U_W = 0.078$ eV). (b) M^3 ESPAT values versus latitude for morning (blue filled circles), noon (red filled circles), and evening (green filled circles) compared to Monte Carlo results (corresponding solid curves). The EPSAT parameter has a linear relationship with surface concentration. The model results for activation energy distributions agree within the standard deviation of the observations. All data shown are reported in Li and Milliken (2017).

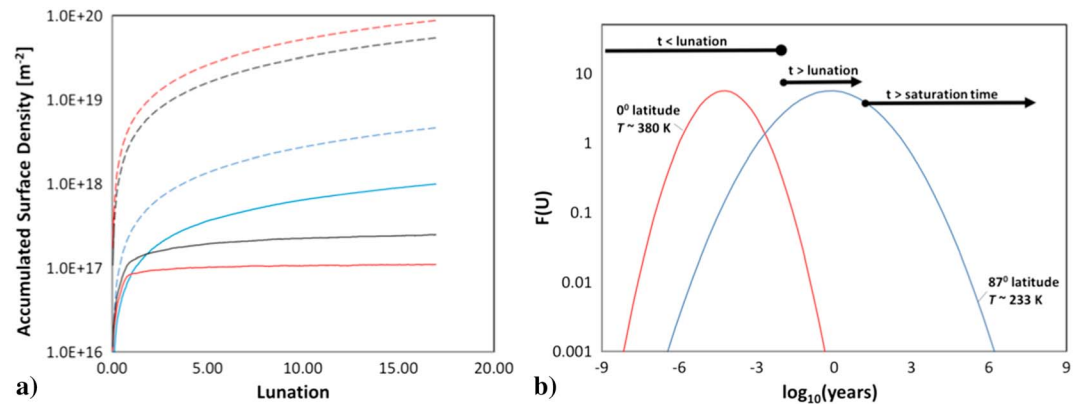


Figure 8. (a) Surface concentration of accumulated hydrogen as a function of time at latitudes of 0° (red), 50° (black), and 87° (blue). The dashed curves show the maximum possible amount of accumulation if all the solar wind protons are implanted, and the solid curves show the simulation results for dynamic equilibrium over 18 lunations. (b) Gaussian distributions of activation energy as a function of diffusion lifetime at latitudes of 0° (red) and 87° (blue) where the $T = 380$ K and 233 K, respectively. At 87° a large fraction the distribution has diffusional lifetimes much longer than the time for saturation. Once the surface is saturated, dynamic equilibrium proceeds with the lower energy trapping sites associated with physical defects.

There may be other ways to create surficial OH, besides via hindered H diffusions. For example, TRIM analyses indicate that every 1 keV proton creates two vacancies and thus two displaced atoms (Farrell et al., 2017). Given that the regolith is ~50% oxygen, then a large population of displaced interstitial O atoms is expected to be present near 10 nm in irradiated silica. These diffusing interstitial O atoms might then find a diffusing H atom to form an interstitial, bonded OH (a stable OH) that migrates to the surface. The solar wind itself implants O ions that form interstitial O that might also find an H to form a stable OH.

Jones et al. (2018) recently described the formation of surficial OH and its possible chemical pathways in the lunar regolith, including the surface creation of water via $\text{OH} + \text{OH} = \text{H}_2\text{O} + \text{O}$. The primary difference between this work and that work is that we follow the H: we consider H diffusion (H only being the mobile atom), the formation of metastable (long-lived) OH pairs around damaged O sites (Fink et al. (1995), and H₂ exospheric emission (Starukhina, 2006). We thus focus on a surface H-exospheric H₂ pathway. In contrast, Jones et al. models a surface OH-exospheric water pathway, with OH being the mobile molecule in the surface. Very likely, both pathways are ongoing simultaneously. Given the copious amounts of H₂ in the exosphere, likely, the H-H₂ pathway dominates; it also becomes clear that the boundary between surface hydrogenation and hydroxylation remains amorphous in our understanding.

We note that Li and Milliken report a larger abundance of hydrogen observed in the Northern Hemisphere. For our prescribed conditions we did not consider effects that would lead to an asymmetric distribution about the equator. Future studies will consider spatial effects due to cold traps, possible polar wander, and lunar mare versus highland surfaces that have undergone varying degrees of space weathering (Wöhler et al., 2017).

It is important to emphasize that we did not consider any additional surface loss processes other than diffusion. As discussed, below ~70° latitude the surface concentration is in equilibrium: balanced by the solar wind influx and H₂ degassing to exosphere. However, at latitudes > ~80° we obtained a net increase in the surface concentration due to the increase in the U/T ratio for lower surface temperatures. As seen in Figure 8b, above ~87° a significant fraction of the activation energy distribution possesses diffusive lifetimes that approach planetary formation timescales. Therefore, at the highest latitudes the surface concentration is limited by the availability of oxygen sites. Following Starukhina (2006), we can estimate an upper limit on the amount of hydrogen that can be trapped to form metastable OH, referred to as the saturation limit. Taking the measured weight percent of oxygen to be ~50% as estimated for the top 60 cm of soil, the corresponding maximum concentration is $\sim 3 \times 10^{28}$ O/m³. Starukhina (2006) reports that 50% of this amount can become bound to hydrogen during implantation giving $\sim 1.5 \times 10^{28}$ O/m³ or >6,000 ppm of OH. This volumetric density represents a near-surface concentration of $\sim 3 \times 10^{20}$ O/m², using $n_s = n_o \cdot h$ for $h = 20$ nm,

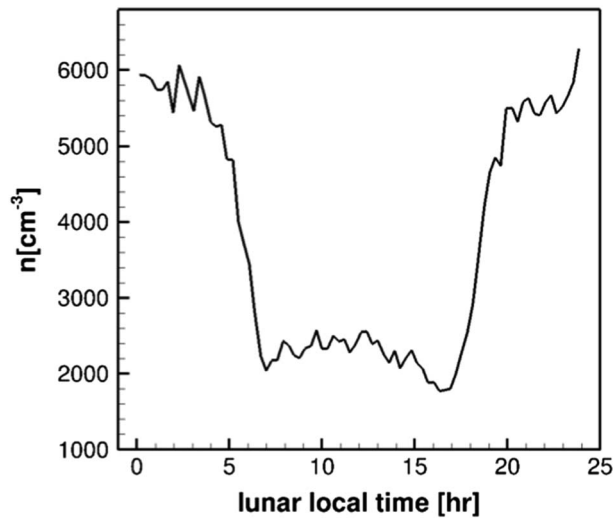


Figure 9. Monte Carlo result of diurnal near-surface H_2 exospheric densities as a function of longitude near 0° latitude from the simulation using $f(U_0 = 0.5 \text{ eV}, U_W = 0.1 \text{ eV})$.

where n_s is the surface concentration and n_o is the concentration of atomic oxygen. We estimated a timeframe of ~ 100 years for saturation using the solar wind flux of $F_{\text{SW}}(87^\circ) = 10^{11} \text{ H/m}^2 \text{ s}$ assuming that all the SW protons are implanted and chemically bond with O. Because our results include a distribution of activation energies characterizing both physical and chemical trapping sites, we obtained a lower accumulation rate of $2 \times 10^{10} \text{ H/m}^2$ corresponding to a saturation lifetime of ~ 500 years. In addition, our estimate of the saturation limit somewhat differs from that in Starukhina (2006) because we use a mean implantation depth of $\sim 20 \text{ nm}$ instead of 100 nm .

At a regional level, Li and Milliken (2017) show evidence that ejecta blankets from new craters have a lower OH content than the surrounding mature soil (e.g., their Figure 3c). One possible interpretation of this observation is that the immature soil has not been exposed long enough to the space environment to become highly damaged (the rim layers might not be fully amorphous). In this case, we might expect quicker diffusion—like that modeled for $U_0 = 0.3 \text{ eV}$ in Figure 3. That is, in the immature soil, the H can more easily migrate and escape to form H_2 .

More studies are needed to understand the trapping efficiency of H atoms in the regolith in order to understand the saturation limits. Additional limiting factors include solar wind reflection, solar wind sputtering, and micrometeoroid vaporization. Wieser et al. (2009) using Chandrayaan-1 observations estimated that up to 20% of the SW is reflected as energetic neutrals. Sputtering and micrometeoroid impacts can also remove surficial OH, but these processes also produce additional damage sites. Nevertheless, once the barrier to OH formation is reached, the distribution of surficial sites has changed and the activation energy distribution effectively shifts from being H retentive to H emissive, more representative of the physical trapping sites (Starukhina & Shkuratov, 2000). For example, consider the high-latitude (blue) curve in Figure 8b. As the hydrogen implants in high U sites, the H is bound for long times in these cold regions, and the H atom will now occupy that high U site, leaving it unavailable for future use. As these high U sites progressively fill in over time, the available sites effectively downshift in energy to the point where the only sites available are those at or faster than lunation timescales. In essence, the average *bulk* activation energy for the blue curve downshifts in time. This distribution evolution process can be included in the model by applying cutoff energy or decreasing the mean energy parameter when the saturation concentration is reached. Both the effective saturation value and the rate at which it progresses are not well constrained.

The results of the H_2 concentration in the exosphere are very consistent with observations from the averaged near-surface densities observed by LAMP. Cook et al. (2013) reported that LAMP observed a density of $\sim 1,700 \text{ cm}^{-3}$ at dusk (18 hr) and $\sim 2,100 \text{ cm}^{-3}$ at dawn (6 hr). A similar asymmetry is shown in the model result in Figure 9. The density distribution produced from a solar wind source of a noncondensable gas will possess local minimums along the terminator reflective of solar flux. However, in our result there is an asymmetry slightly enhanced by the effect of the diffusion on the local source rate of degassing hydrogen near the dawn (6 hr) and dusk (18 hr) terminators. On the nightside the result is typical for an exosphere in thermal equilibrium with the surface, and the maximum density obtained was $\sim 6,000 \text{ cm}^{-3}$. The H_2 density on the nightside of the Moon is not well constrained by observation. Hoffman et al. (1973) report a density of $\sim 65,000 \text{ cm}^{-3}$ from the Apollo 17 Lunar Atmospheric Composition Experiment, but it is not clear if that measurement was an artifact due to instrument outgassing (Hodges, 1973). Further observations of the exospheric distribution on the nightside and terminator may provide verification of a diffusing source of molecular hydrogen. In the future such observations may be useful for deriving additional constraints on the inventory of H_2 degassed from the surface.

In general, diffusion-limited degassing may play an important role on the distribution of molecular gases in the exospheres of airless bodies. If the lifetimes are comparable to that of atmospheric loss processes such as escape and photodestruction, the exospheric abundance will be limited by diffusion.

4. Conclusions

Hydroxylation by solar wind implantation remains a plausible explanation of the 3- μm feature observed broadly over the lunar surface. Leveraging the statistical mechanics formalism presented in Farrell et al. (2017), we applied the activation energy distributions to a Monte Carlo test particle model. Our nominal results were obtained using an activation energy distribution, $f(U_0 = 0.5 \text{ eV}, U_W = 0.078 \text{ eV})$. We adopted physically derived parameters based on experiments of H_2 degassing from irradiated silica, $D_0 = 10^{-12} \text{ m}^2/\text{s}$, $U_W = 0.1 \text{ eV}$, and $U_0 = 0.3\text{--}0.7 \text{ eV}$ (Devine, 1985; Fink et al., 1995; Shelby & Keeton 1974). The key difference between this study and the previous studies of Farrell et al. (2015, 2017) is that we (1) modeled the spatial distribution of the surface concentration and (2) we tracked the rate of change of this distribution as a function of lunation. Most of the hydrogen delivered to the surface from the solar wind is lost to the exosphere and escape on timeframes less than a lunation. However, when using the same activation energy distribution $f(U_0 = 0.5 \text{ eV}, U_W = 0.1 \text{ eV})$, we obtained much larger surface concentrations. We conclude that the fractional population of implanted H atoms with activation energies $>0.5 \text{ eV}$ is important to consider in calculations of the surface concentration for comparisons to observations of the IR absorption signature, because this fraction undergoes very slow diffusion and is not involved in the immediate sublunation diffusive process.

We note that the $U_0 = 0.5 \text{ eV}$ case in Figure 5 has a resemblance to the surface IR observations of Li and Milliken (2017) and is consistent with the exospheric content of H_2 observed by LAMP. There is a third anchoring point to examine: The equilibrium of global H content. Specifically, the solar wind source rate to the surface is $\sim 32 \text{ g/s}$, and the nominal distribution ($U_0 = 0.5 \text{ eV}$) results in a dayside degassing rate of $\sim 27 \text{ g/s}$ for H_2 . These values are comparable and suggest that the solar wind proton source and outgassing loss are in dynamic equilibrium across the globe. Distributions centered at values of $U_0 > 0.52 \text{ eV}$ increasingly limit exospheric content because the surface diffusion lifetime is longer and the rate of H_2 outgassing limits the removal of hydrogen from the system by thermal escape. For example, for $U_0 \sim 0.7 \text{ eV}$, the degassing rate was only 13 g/s , suggesting that there is an excessive hydrogen buildup in the surface—which is not observed (and thus rules out the higher activation energy cases). Taking into consideration the global-averaged H content, there has to be some evidence of a diurnal effect in order to have the H content of the system in equilibrium with the solar wind source—as reported in Li and Milliken. This result has implications for other solar wind-derived species that degas at rates lower than the solar loss rate.

We assumed that all incident protons are converted to OH. However, Zeller et al. (1966) placed broad bounds (10%–100%) on the amount of incident protons that are converted to OH. Another pathway for hydrogen loss is the formation of CH_4 in the regolith and subsequently loss to the exosphere. Hodges (2016) reported on LADEE observations of $\sim 450 \text{ cm}^{-3}$ of CH_4 in the lunar exosphere near sunrise at an altitude of 12 km . Given the damage caused by irradiation, we also anticipate a population of displaced, interstitial atomic oxygen that are no longer bound to Si or a parent metal (Fe-, Ti-, etc.) in the crystal matrix. These interstitial O atoms could strongly bond to a diffusing H atom to make a stable, independent OH molecule. This population would also contribute to the $2.8\text{-}\mu\text{m}$ IR absorption.

Thus, an important bound to constraining this approach is to understand the various pathways and limits of hydroxyl formation. Molecular Dynamics (MD) simulations could be a useful tool for investigating the dynamics of ion sputtering and thermal spike sputtering (Tucker et al., 2005) of regolith-like (SiO_2) grains leading to OH formation. MD studies could provide results on ejecta distributions, trapping efficiencies, and weathering rates that can be directly applied to surface bound exosphere models (Cassidy et al., 2009).

It is important to note that recent studies reveal the analyses of M^3 reflectance spectra depend on the assumed thermal correction used to account for surface roughness and thermal emissions (Bandfield et al., 2018). For example, Bandfield et al. applied a physics-based thermal correction and found the OH absorption signature to be prominent at all latitudes and times of day. They also consider solar wind implantation of H^+ as the predominate process resulting in the formation of OH. Consistent with Bandfield et al., our model result indicates that proton implantation can account for the presence of a widespread OH signature. However, we obtained both a latitudinal and diurnal distributions of hydroxyl more consistent with Li and Milliken (2017). We attribute this result to the ratio of U/T and not solely to local surface temperature (Farrell et al., 2017). It is not clear what physical processes would lead to uniform hydroxylation at all

latitudes. As demonstrated in our Case 2 due to lower solar flux at high latitudes, one would expect a weaker absorption at high latitudes compared to low latitudes if implantation at all latitudes predominantly results in the trapping of OH. However, monitoring such a variation may currently be out of our observational limits (Bandfield et al. 2018).

When applying a similar correction to the M^3 spectra, Wöhler et al. (2017) also found that there was significant concentration of hydroxyls at all latitudes. Contrary to Bandfield et al., they reported the presence of diurnal effects noting a larger day-night variation at high latitudes compared to low latitudes. We also obtain this trend at midlatitudes compared to low latitudes as shown in Figure 5a. It is interesting that despite this diurnal variation, they find little variation in concentration with latitude at midday. This finding is different from the analyses of Li and Milliken that report a significant latitudinal dependence as shown in Figure 7, which the results herein support. Wöhler et al. reported that their analyses are consistent with there being a combination of both solar-produced OH and a strongly bound endogenous source. The models presented here did not include an endogenous source of OH, but Case 2 may offer insight on the expected result. For example, in Case 2 the prescribed activation energy distribution resulted in surface being H retentive, and there was a buildup of a large background OH concentration near the saturation limit of $>\sim 6,000$ ppm. Within this limit the background density masked all diurnal variations. If a diurnal variation is present with an endogenous source, the background concentration cannot be significantly larger than the implanted density over a lunation.

While there is general agreement that the solar wind is producing a hydroxyl signature on the Moon, the dominant processes leading to the signature and its global distribution are still under investigation. We have shown that if hydrogen were not degassed at a rate similar to the implantation rate, a significant amount of water would accumulate on the surface, which is not observed. A global hydrogen layer that is not dynamically changing suggests a buildup of hydrogen over long times. Our results support there being a global-scale dynamic equilibrium of the hydrogen consistent with the Li and Milliken (2017) findings. Nevertheless, the diffusion-based models presented herein or the reaction rate models presented in Jones et al. (2018) are useful tools to constrain theory with observational and experimental data.

Acknowledgments

The model data used to produce the results can be accessed in the supporting information provided. The authors acknowledge Dr. Larissa Starukhina for very useful discussions. O. J. Tucker acknowledges support of this work from the NASA Postdoctoral Program, the DREAM2 team and SSERVI, and computational resources provided by the University of Virginia HPC system Rivanna.

References

- Acharyya, K. (2014). Laboratory study of sticking and desorption of H_2 and its significance in the chemical evolution of dense interstellar medium. *Monthly Notices of the Royal Astronomical Society*, *443*(2), 1301–1309. <https://doi.org/10.1093/mnras/stu1219>
- Bandfield, J. L., Poston, M. J., Kilma, R. L., & Edwards, C. S. (2018). Widespread distribution of OH/H₂O on the lunar surface inferred from spectral data. *Nature Geoscience*, *11*, 173–177. <https://doi.org/10.1038/s41561-018-0065-0>
- Brinkmann, R. T. (1970). Departures from Jeans' escape rate for H and He in the Earth's atmosphere. *Planetary and Space Science*, *18*(4), 449–478. [https://doi.org/10.1016/0032-0633\(70\)90124-8](https://doi.org/10.1016/0032-0633(70)90124-8)
- Butler, B. J. (1997). The migration of volatiles on the surfaces of Mercury and the Moon. *Journal of Geophysical Research*, *102*(E8), 283–291.
- Cassidy, T. A., Johnson, R. E., & Tucker, O. J. (2009). Trace constituents of Europa's atmosphere. *Icarus*, *201*(1), 182–190. <https://doi.org/10.1016/j.icarus.2008.12.033>
- Clark, R. N. (2009). Detection of adsorbed water and hydroxyl on the Moon. *Science*, *326*(5952), 562–564. <https://doi.org/10.1126/science.1178105>
- Cook, J. C., Alan Sterna, S., Feldman, P. D., Randall Gladstone, G., Retherford, K. D., & Tsang, C. C. C. (2013). New upper limits on numerous atmospheric species in the native lunar atmosphere. *Icarus*, *225*(2013), 681–687.
- Crider, D. H., & Vondrak, R. R. (2002). Hydrogen migration to the lunar poles by solar wind bombardment of the Moon. *Advances in Space Research*, *30*(8), 1869–1874. [https://doi.org/10.1016/S0273-1177\(02\)00493-3](https://doi.org/10.1016/S0273-1177(02)00493-3)
- Crider, D. M., & Vondrak, R. R. (2000). *Journal of Geophysical Research*, *105*(26), 773–782.
- Devine, R. A. B. (1985). The role of activation energy distributions in diffusion related annealing in SiO₂. *Journal of Applied Physics*, *58*(2), 716–719. <https://doi.org/10.1063/1.336187>
- Farrell, W. M., Hurley, D. M., Esposito, V. J., McLain, J. L., & Zimmerman, M. I. (2017). The statistical mechanics of solar wind hydroxylation at the Moon, within lunar magnetic anomalies, and at Phobos. *Journal of Geophysical Research: Planet*, *122*, 269–289. <https://doi.org/10.1002/2016JE005168>
- Farrell, W. M., Hurley, D. M., & Zimmerman, M. I. (2015). Solar wind implantation into lunar regolith: Hydrogen retention in a surface with defects. *Icarus*, *255*, 116–126. <https://doi.org/10.1016/j.icarus.2014.09.014>
- Feldman, P. D., & Morrison, D. (1991). The Apollo 17 ultraviolet spectrometer: Lunar atmosphere measurements revisited. *Geophysical Research Letters*, *18*(11), 2105–2108. <https://doi.org/10.1029/91GL01998>
- Fink, D., Krauser, J., Nagengast, D., Murphy, T. A., Erxmeier, J., Palmetshofer, L., et al. (1995). Hydrogen implantation and diffusion in silicon and silicon dioxide. *Applied Physics A: Materials Science & Processing*, *61*(4), 381–388. <https://doi.org/10.1007/BF01540112>
- Griscom, D. L. (1984). Thermal bleaching of X-ray-induced defect centers in high purity fused silica by diffusion of radiolytic molecular hydrogen. *Journal of Non-Crystalline Solids*, *68*(2-3), 301–325. [https://doi.org/10.1016/0022-3093\(84\)90013-9](https://doi.org/10.1016/0022-3093(84)90013-9)
- Halekas, J. S., Benna, M., Mahaffy, P. R., Elphic, R. C., Poppe, A. R., & Delory, G. T. (2015). Detections of lunar exospheric ions by the LADEE neutral mass spectrometer. *Geophysical Research Letters*, *42*, 5162–5169. <https://doi.org/10.1002/2015GL064746>
- Hartle, R. E., & Thomas, G. E. (1974). Neutral and ion exosphere models for lunar hydrogen and helium. *Journal of Geophysical Research*, *79*(10), 1519–1526. <https://doi.org/10.1029/JA079i010p01519>

- Hodges, R. R. (1973). Helium and hydrogen in the lunar atmosphere. *Journal of Geophysical Research*, 78(34), 8055–8064. <https://doi.org/10.1029/JA078i034p08055>
- Hodges, R. R. (2016). Methane in the lunar exosphere: Implications for solar wind carbon escape. *Geophysical Research Letters*, 43, 6742–6748. <https://doi.org/10.1002/2016GL068994>
- Hodges, R. R., & Johnson, F. S. (1968). Lateral transport in planetary exospheres. *Journal of Geophysical Research*, 73(23), 7307–7317. <https://doi.org/10.1029/JA073i023p07307>
- Hoffman, J. H., Hodges, R. R., & Evans, D. E. (1973). Lunar atmospheric composition results from Apollo 17, Proc. Fourth Lunar Sci. Conf. *Geochimica et Cosmochimica Acta*, 4(3), 2865.
- Huebner, W. F., & Mukherjee, J. (2015). Photoionization and photo-dissociation rates in solar and blackbody radiation fields. *Planetary and Space Science*, 106, 11–45. <https://doi.org/10.1016/j.pss.2014.11.022>
- Hurley, D. M., Cook, J. C., Retherford, K. D., Greathouse, T. K., Gladstone, G. R., Mandt, K., et al. (2016). Contributions of the solar wind and micro-meteoroids to molecular hydrogen in the lunar exosphere. *Icarus*, 283, 31–37.
- Johnson, F. (1971). Lunar atmosphere. *Reviews of Geophysics*, 9(3), 813. <https://doi.org/10.1029/RG009i003p00813>
- Johnson, R. E. (1990). *Energetic charged particle interactions with atmospheres and surface*. New York: Springer. <https://doi.org/10.1007/978-3-642-48375-2>
- Jones, B. M., Aleksandrov, A., Hibbitts, K., Dyar, M. D., & Orlando, T. M. (2018). Solar wind-induced water cycle on the Moon. *Geophysical Research Letters*, 45, 10,959–10,967. <https://doi.org/10.1029/2018GL080008>
- Lee, R. W. (1963). Diffusion of hydrogen in natural and synthetic fused quartz. *The Journal of Chemical Physics*, 38(2), 448–455. <https://doi.org/10.1063/1.1733679>
- Lee, R. W. (1964). *Physics and Chemistry of Glasses*, 5, 35–43.
- Li, S., & Milliken, R. E. (2017). Water on the surface of the Moon as seen by the Moon Mineralogy Mapper: Distribution, abundance, and origins. *Science Advances*, 3, e170147. <https://doi.org/10.1126/sciadv.1701471>
- Mattern, P. L., Thomas, G. J., & Bauer, W. (1976). Hydrogen and helium implantation in vitreous silica. *Journal of Vacuum Science and Technology*, 13(1), 430–436. <https://doi.org/10.1116/1.568938>
- McKay, D. S., Heiken, G., Basu, A., Blanford, G., Simon, S., Reedy, R., et al. (1991). The lunar regolith. In G. H. Heiken, D. T. Vaniman, & B. M. French (Eds.), *The lunar sourcebook*, (pp. 285–356). New York NY: Cambridge Univ. Press.
- Penteado, E. M., Walsh, C., & Cuppen, H. M. (2017). Sensitivity analysis of grain surface chemistry to binding energies of ices species. *Astrophysics Journal*, 844(1), 71, 13pp. <https://doi.org/10.3847/1538-4357/aa78f9>
- Pieters, C. M., Goswami, J. N., Clark, R. N., Annadurai, M., Boardman, J., Buratti, B., et al. (2009). Character and spatial distribution of OH/H₂O on the surface of the Moon seen by M³ on Chandrayaan-1. *Science*, 326(5952), 568–572. <https://doi.org/10.1126/science.1178658>
- Revesz, A. G. (1979). The role of hydrogen in SiO₂ films on silicon. *Journal of the Electrochemical Society*, 126(1), 122–130. <https://doi.org/10.1149/1.2128967>
- Shelby, J. E., & Keeton, S. C. (1974). Temperature dependence of gas diffusion in glass. *Journal of Applied Physics*, 45(3), 1458–1460. <https://doi.org/10.1063/1.1663433>
- Starukhina, L. V. (2006). Polar regions of the Moon as a potential repository of solar-wind implanted gases. *Advances in Space Research*, 37(1), 50–58. <https://doi.org/10.1016/j.asr.2005.04.033>
- Starukhina, L. V. (2012). Water on the Moon: What is derived from the observations? In V. Badescu (Ed.), *Moon: Prospective energy and material resources*. NY: Springer-Verlag. https://doi.org/10.1007/978-3-642-27969-0_3
- Starukhina, L. V., & Shkuratov, Y. G. (2000). The lunar poles: Water ice or chemically trapped hydrogen. *Icarus*, 147(2), 585–587. <https://doi.org/10.1006/icar.2000.6476>
- Stern, S. A., Cook, J. C., Chaufray, J.-Y., Feldman, P. D., Randall Gladstone, G., & Retherford, K. D. (2013). Lunar atmospheric H₂ detections by the LAMP UV spectrograph on the Lunar Reconnaissance Orbiter. *Icarus*, 226(2), 1210–1213. <https://doi.org/10.1016/j.icarus.2013.07.011>
- Sunshine, J. M., Farnham, T. L., Feaga, L. M., Groussin, O., Merlin, F., Milliken, R. E., & A'Hearn, M. F. (2009). Temporal and spatial variability of lunar hydration as observed by the Deep Impact spacecraft. *Science*, 326(5952), 565–568. <https://doi.org/10.1126/science.1179788>
- Tenishev, V., Rubin, M., Orenthal, J., Combi, M. R., & Sarantos, M. (2013). Kinetic modeling of sodium in the lunar exosphere. *Icarus*, 226(2), 1538–1549. <https://doi.org/10.1016/j.icarus.2013.08.021>
- Thampi, S. V., Sridharan, R., Das, T. P., Ahmed, S. M., Kamalakar, J. A., & Bhardwaj, A. (2015). The spatial distribution of molecular hydrogen in the lunar atmosphere—New results. *Planetary and Space Science*, 106, 142–147. <https://doi.org/10.1016/j.pss.2014.12.018>
- Tucker, O. J., Ivanov, D. S., Zhigilei, L. V., Johnson, R. E., & Bringa, E. M. (2005). Molecular dynamics simulation of sputtering from a cylindrical track: EAM versus pair potentials. *Nuclear Instruments and Methods B*, 228(1-4), 163–169. <https://doi.org/10.1016/j.nimb.2004.10.040>
- Tucker, O. J., Johnson, R. E., & Young, L. A. (2015). Gas transfer in the Pluto-Charon system: A Charon atmosphere. *Icarus*, 246, 291–297. <https://doi.org/10.1016/j.icarus.2014.05.002>
- Turkevich, A. L. (1973). *The Moon*, 8(3), 365–367. <https://doi.org/10.1007/BF00581730>
- Wieser, M., Barabash, S., Futaana, Y., Holmström, M., Bhardwaj, A., Sridharan, R., et al. (2009). Extremely high reflection of solar wind protons as neutral hydrogen atoms from regolith in space. *Planetary and Space Science*, 57(14-15), 2132–2134. <https://doi.org/10.1016/j.pss.2009.09.012>
- Williams, R. J., & Jadwick, J. J. (1980). *Handbook of lunar materials*. NASA RP-1057, (p. 120). Washington: NASA.
- Wöhler, C., Grumpe, A., Berezhnoy, A. A., & Shevchenko, V. V. (2017). Time-of-day-dependent global of lunar surficial water/hydroxyl distribution. *Science Advances*, 3, e1701286.
- Zeller, E. J., Ronca, L. B., & Levy, P. W. (1966). Proton-induced hydroxyl formation on the lunar surface. *Journal of Geophysical Research*, 71(20), 4855–4860. <https://doi.org/10.1029/JZ071i020p04855>